

# Tunable Color Filters Based on Metal–Insulator–Metal Resonators

Kenneth Diest,<sup>\*,†</sup> Jennifer A. Dionne,<sup>†</sup> Merrielle Spain,<sup>‡</sup> and Harry A. Atwater<sup>†</sup>

*Thomas J. Watson Laboratory of Applied Physics, Department of Computation and Neural Systems, California Institute of Technology, Pasadena, California, 91125*

*Received March 10, 2009; Revised Manuscript Received May 14, 2009*

## ABSTRACT

We report a method for filtering white light into individual colors using metal–insulator–metal resonators. The resonators are designed to support photonic modes at visible frequencies, and dispersion relations are developed for realistic experimental configurations. Experimental results indicate that passive Ag/Si<sub>3</sub>N<sub>4</sub>/Au resonators exhibit color filtering across the entire visible spectrum. Full field electromagnetic simulations were performed on active resonators for which the resonator length was varied from 1–3  $\mu\text{m}$  and the output slit depth was systematically varied throughout the thickness of the dielectric layer. These resonators are shown to filter colors based on interference between the optical modes within the dielectric layer. By careful design of the output coupling, the resonator can selectively couple to intensity maxima of different photonic modes and, as a result, preferentially select any of the primary colors. We also illustrate how refractive index modulation in metal–insulator–metal resonators can yield actively tunable color filters. Simulations using lithium niobate as the dielectric layer and the top and bottom Ag layers as electrodes, indicate that the output color can be tuned over the visible spectrum with an applied field.

Today, color filters are a key component in digital photography, digital projectors, and computer displays, and current research on color filtering is focused on developing smaller, faster, and lower power designs. One approach to meeting these challenges is the use of plasmonic resonators that couple incident light into electromagnetic modes that propagate along a metal–dielectric interface. Because of the ability to integrate electrodes in a straightforward manner, metal–insulator–metal (MIM) waveguides<sup>1–4</sup> are of considerable interest for electro-optic device applications. MIM waveguides enable subwavelength spatial mode confinement and propagation lengths of 1–40  $\mu\text{m}$  in the visible and near-infrared spectrum. Both passive and active MIM waveguides have received increasing attention<sup>5</sup> because the top and bottom metal layers in an MIM waveguide can serve as both cladding layers and electrodes. These devices can support both photonic modes, whose mode momentum is less than the free space photon momentum and plasmonic modes whose mode momentum is larger than the free space photon momentum.<sup>3</sup> In the present work, we exploit the ability of MIM resonators to support several photonic modes with frequencies that correspond to the primary colors, enabling these resonators to act as color filters.

Color filtering is currently one of many areas where passive photonic<sup>6</sup> and plasmonic<sup>7–9</sup> devices are being explored for spectral imaging applications. By varying the

refractive index and thickness of the dielectric layer within MIM resonators, as well as the geometries of the in- and out-coupling structures, the spectral transmittance can be tuned over a wide range. The resonator geometry allows the output slit to be designed so as to preferentially couple out any of the supported optical modes. In addition, because these resonators are on the order of 1–5  $\mu\text{m}$  in length, they provide a unique opportunity to design color filters whose resolution and areal density are significantly higher than those currently available. In prototype designs for active plasmonic devices, electro-optic materials such as lithium niobate are being explored. Because lithium niobate has a large electro-optic coefficient, it is used extensively in surface acoustic wave devices and optical modulators.<sup>10,11</sup>

Here we report a method for filtering white light into individual colors using passive and active MIM resonators. These devices take advantage of the fact that the resonators filter out colors based on interference and resonances between the optical modes within the cavity. By careful design of the depth and location of resonator output slits, it is possible to preferentially couple to the different photonic modes and select any of the primary colors. In addition, by taking advantage of the electro-optic effect in lithium niobate, the specifically selected output color can be tuned over a wide range with an applied field.

**Results and Discussion.** A schematic diagram of the MIM resonator geometry used is shown in Figure 1. This structure has input and output slits milled into the top and bottom cladding layers, respectively. The separation between the input and output slits is labeled “ $d_{\text{sep}}$ ”, and the depth to which

\* To whom correspondence should be addressed. E-mail: diest@caltech.edu.

<sup>†</sup> Thomas J. Watson Laboratory of Applied Physics.

<sup>‡</sup> Computation and Neural Systems.

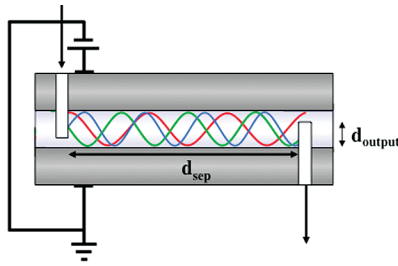


**Figure 1.** A schematic diagram of the MIM geometry used with input and output slits placed on the top and bottom of the waveguide (a). Depicted within the dielectric layer of (a) are the red, green, and blue photonic modes of the MIM waveguide. The spacing between input and output slits is labeled  $d_{sep}$ , and the output slit's depth into the dielectric layer is labeled as  $d_{output}$ .

the output slit is etched into the lithium niobate is labeled “ $d_{output}$ ”. For all simulations and experiments, plane wave white light illumination in the wavelength range  $\lambda = 400\text{--}700\text{ nm}$  is sent through the input slit, traverses the length of the optical cavity, and is detected after exiting the output slit.

To calculate the color that a viewer would observe at the device output, the CIE (1964) color matching functions were used to correlate the chromatic response of the color-sensitive cones within the eye of a viewer over the visible range of the MIM output spectrum.<sup>12</sup> The red, green, and blue spectral sensitivity curves of the human eye are shown from 400–700 nm (see Supporting Information). The transmitted optical power spectrum through the output slit of each device was recorded. For finite-difference time domain simulations of these structures, the output power was normalized to the source power at each wavelength. The resulting color output was calculated by taking the inner product of each of the R, G, and B color matching functions with the optical intensity from a specific device over the entire visible spectrum.<sup>13</sup> Then color scales were developed that illustrated the output color seen by a viewer.

Experimental measurements of passive structures showed color filtering across the red, green, and blue regions of the visible spectrum. The devices shown in Figure 2a consist of a 500 nm silicon nitride freestanding membrane coated on top with 400 nm of gold and with 400 nm of silver on the bottom side of the membrane. Input and output slits were defined by 20 keV  $\text{Ga}^+$  ions in a focused ion beam lithography etching system. The devices were illuminated with a halogen white light source, and colors were recorded by color imaging in an optical microscope with a 50 $\times$  objective using a digital camera. In Figure 2a, each device exhibits a different color at its output slit, and the colors shift across the entire visible spectrum as a function of the spacing between the input and output slits. Here the resonator length  $d_{sep} = 2.5, 3.5,$  and  $4\ \mu\text{m}$  for devices 1–3, respectively, with a slit width of 400 nm. For all devices shown in Figure 2a, the slit depths were  $d_{input} = d_{output} = 250\text{ nm}$ . The corresponding output spectra from these devices are shown in Figure 2b. For each curve in Figure 2b, the color corresponds to the RGB value calculated using the method described in the previous paragraph with each output spectrum shown in Figure 2b. The fact that the calculated

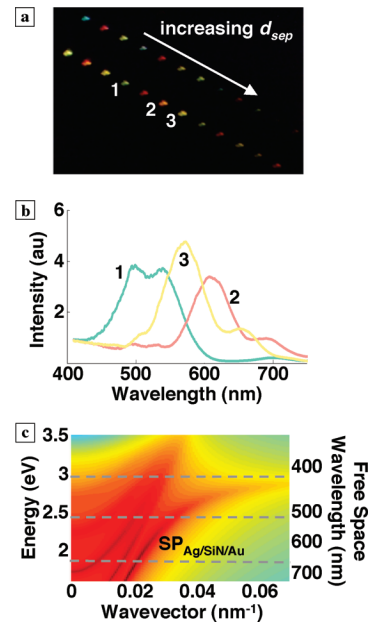


**Figure 2.** An example of color filtering in passive MIM waveguides is shown in (a). This structure consists of 400 nm of silver as the top layer, 500 nm of silicon nitride as the dielectric, and 400 nm of gold as the bottom layer. Devices 1–3 have  $d_{sep} = 2.5, 3.5,$  and  $4\ \mu\text{m}$  respectively. The corresponding output spectra are shown in (b). The RGB color of each curve was calculated using the method described in the manuscript, and the colors for a given device in Figure 2a and 2b are equivalent. The dispersion diagram for these structures is plotted in (c) and shows the plasmonic and three photonic modes within the visible spectrum.

color from the device output spectrum is the same as the experimentally observed color confirms that the output spectrum were correctly converted into an equivalent observable color. The dispersion diagram for this structure is shown in Figure 2c. Regions of the dispersion diagram that have a high photonic or plasmonic modal intensity appear darker (red and gray/black) and regions with little or no modal intensity appear lighter (green and blue). Figure 2c shows the existence of three photonic modes and one plasmonic mode across the visible spectrum. These dispersion diagrams were calculated using a Nelder-Mead minimization of numerical solutions to Maxwell’s equations.<sup>14</sup>

To model active devices, simulations were done using Lumerical, finite-difference time-domain software. The structures used in the simulations had 400 nm of silver on the top and bottom of the waveguide with 300 nm of lithium niobate as the dielectric layer. The devices were simulated under broadband transverse magnetic illumination from  $\lambda = 400\text{--}700\text{ nm}$ . All simulations were done with and without an applied electric field.

X-cut lithium niobate single crystal samples were obtained from the MTI Corporation. Using spectroscopic ellipsometry, the complex index of refraction of the lithium niobate was measured, and this data was used for all simulations. The top and bottom silver layers of the MIM waveguide were modeled using the materials parameters within the Lumerical materials database. The experimental lithium niobate data was fit from 400–700 nm as a Cauchy layer given by

$$n(\lambda) = n_0 + C_0 \frac{n_1}{\lambda^2} + C_1 \frac{n_2}{\lambda^4} \quad (1)$$

$$k(\lambda) = k_0 + C_0 \frac{k_1}{\lambda^2} + C_1 \frac{k_2}{\lambda^4} \quad (2)$$

where  $n_0 = 2.093$ ,  $n_1 = 305.9$ ,  $n_2 = 52.9$ ,  $k_0 = -0.02$ ,  $k_1 = -24.541$ ,  $k_2 = -23.276$ ,  $C_0 = 10^2$ ,  $C_1 = 10^7$ , and  $\lambda$  is given in nanometers. The reported coercive field for this material is  $\sim 4$  kV/mm;<sup>16</sup> under an applied electric field greater than this the lithium niobate was modeled as having a refractive index increase of  $\sim 0.12$  across the visible spectrum, and the imaginary part of the index was kept the same as in the zero field case. This change in refractive index is consistent with domain switching in ferroelectric lithium niobate crystals.<sup>17</sup>

For all simulations involving lithium niobate,  $d_{\text{input}} = 150$  nm. Simulations show that by holding  $d_{\text{input}}$  and  $d_{\text{output}}$  constant while varying  $d_{\text{sep}}$ , the intensity of the most efficiently out-coupled color oscillates as the output slit couples to either a maximum or minimum in the selected color's electric field. Figure 3 shows the colors from devices with  $d_{\text{output}} = 260$  nm and  $d_{\text{sep}}$  is varied from 1–3  $\mu\text{m}$  in 50 nm steps. The top color stripe corresponds to devices under no applied electric field and the bottom color stripe corresponds to devices under an applied field. With no applied field, oscillations between the green and red modes can be seen. It can also be seen that when  $d_{\text{sep}}$  is such that the red mode is at a minimum, the green mode is most efficiently coupled through the output slit. Conversely, when the intensity of the red mode is a maximum, it is most efficiently coupled through the output slit and dominates the device transmission. By applying an electric field, the red mode dominates the device transmission and the resulting colors appear red shifted.

Figure 3b shows the normalized power transmission through the devices from Figure 3a. The top pane corresponds to transmission under no applied electric field and the bottom pane corresponds to transmission under an applied field. The transmission at three representative wavelengths of 450, 531.5, and 649.2 nm were selected from the entire visible spectrum and were plotted in blue, green, and red, respectively. As was mentioned above, when  $d_{\text{sep}}$  is such that the red mode is at a minimum, the green mode is most efficiently coupled through the output slit. The lower transmission plot shows that with an applied field, the transmission of the green mode is suppressed with respect to that of the red and blue modes. As a result, the dominant green oscillations that are seen in the top color stripe of Figure 3a are no longer present in the bottom color stripe of Figure 3a.

The source of the oscillations seen in Figure 3b is different for each of the three wavelengths sampled. For these MIM waveguides, the 200 nm wide output slit acts as a convolution function when it “samples” the optical modes by coupling them out of the device. The oscillations at 650 nm are from the slit coupling to maxima and minima of the mode as  $d_{\text{sep}}$  is varied from 1–3  $\mu\text{m}$ . For the intensity at 530 nm, the “convolution length” of the slit is on the order of half the

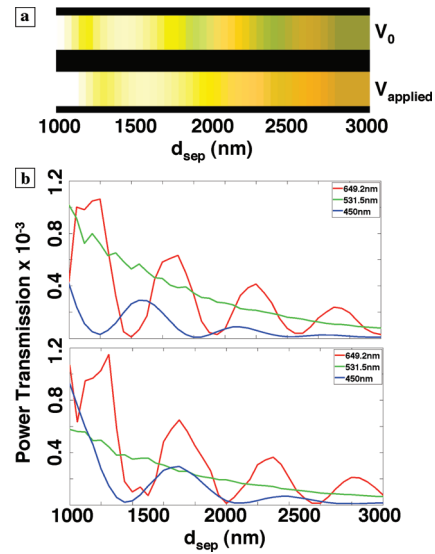


**Figure 3.** Output colors from MIM waveguides with  $d_{\text{input}} = 150$  nm into the top half of the lithium niobate layer and  $d_{\text{output}} = 260$  nm into the lithium niobate layer from the bottom of the structure. The output colors are plotted as a function of the spacing between the input and output slits. The bottom stripe of color is for devices under an applied field and the top stripe of color is for devices under no applied field. The normalized power transmission through these devices is shown in (b). The top pane is transmission with no applied field and the lower pane is with an applied electric field. The transmission at three representative wavelengths of 450, 531.5, and 649.2 nm were selected from the entire visible spectrum.

wavelength of the mode being sampled. As a result, there are small oscillations in the output intensity as  $d_{\text{sep}}$  is varied; however, any major oscillations are damped out as a result of the slit width. Hence, the main shape of the green curve is simply determined by the decay of the mode as  $d_{\text{sep}}$  is increased. The oscillations of the blue curve result from beating between two modes propagating at 450 nm. Since this beating period is much larger than the actual period of either of the two modes involved, the oscillations can again be resolved by the 200 nm output slit.

Figure 3b also shows that for a given resonator, the transmitted power at a given wavelength is on the order of 0.05%; however, this metric is best suited for devices that transmit a single or narrow band of wavelengths. In the case of these MIM color filters, the resonators pass a broadband spectrum. When this intensity spectrum is integrated with the RGB color matching functions over the entire visible spectrum, the total amount of transmitted power is significantly increased. Future work will be focused on optimizing the design of the input and output slits to increase the total amount of transmitted power; however, initial results indicate that the total broadband transmitted power can be increased by at least an order of magnitude.

Modeling the dispersion of the MIM waveguides shows the existence of the plasmonic and three photonic modes, as illustrated in Figure 4a, which is a plot of the frequency dependence of the real part of the wavevector. For a lithium niobate layer 300 nm thick, the dispersion calculations show that the structure's three photonic modes lie in the regions 1.9, 2.5, and 3 eV, which correspond to the red, green, and

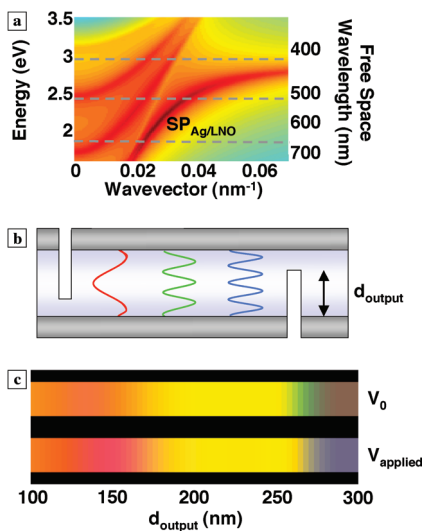


**Figure 4.** The dispersion diagram for the MIM structure with 300 nm of lithium niobate between two, 400 nm layers of silver, (a). The plot shows the plasmonic and three photonic modes that lie in the red, green, and blue regions of the visible spectrum. By adjusting the output slit depth, the device will selectively couple to the red, green, or blue photonic modes. These mode profiles are plotted within the MIM structure in (b). Not shown here is the mode profile of either the symmetric or antisymmetric plasmon mode. The resulting output colors from a MIM waveguide with an input-output slit spacing of 2000 nm are shown in (c). The top stripe of color is for devices under no applied field and the bottom stripe is for devices under an applied field.

blue regions of the visible spectrum, respectively. Figure 4b shows the red, green, and blue photonic mode profiles moving through the MIM waveguide. Not shown here is the mode profile of either the symmetric or antisymmetric plasmon modes. The MIM waveguides modeled in Figure 4c had a constant  $d_{\text{sep}} = 2000$  nm for all devices with and without an applied electric field. For these simulations,  $d_{\text{output}}$  was increased from 100–300 nm into the lithium niobate in 2 nm increments from one colored panel to another in Figure 4c. By simply varying the depth of the output slit into the lithium niobate layer, one can preferentially couple to the different photonic modes and output any of the primary colors. In Figure 4c, the top color stripe corresponds to no applied electric field and the bottom color stripe corresponds to devices under an applied field. For these specific devices, the output slit most efficiently couples to the red mode with and without an applied electric field for slit depths below  $\sim 150$  nm. With no applied electric field, the output slit most efficiently couples to the green mode between 250 and 275 nm, and with an applied field the output slit most efficiently couples to the blue mode above  $\sim 285$  nm.

To further increase the total amount of light transmitted through the waveguides, the design scheme presented here could be easily integrated into a high density array of metal–insulator–metal resonator color filters. By fabricating two output slits equally spaced on either side of an input slit, one could double the total amount of transmitted light. By close packing three of these structures together with three input slits, each rotated by  $\pm 120^\circ$  with respect to the other two, a hexagonal “MIM pixel” could be produced. A cross-

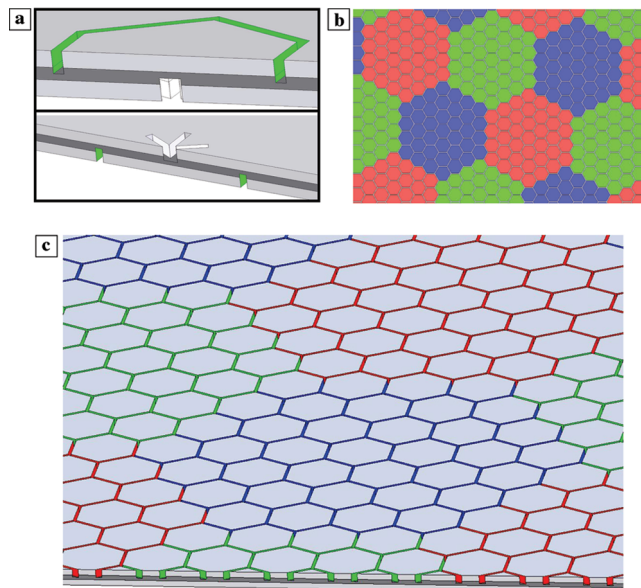


**Figure 5.** Cutaway view of a six-sided MIM color filter (a). The top panel shows half of the hexagonal output structure while the bottom panel shows half of the three-slit input configuration for a given hexagon. (b) Tiling layout for a red–green–blue “superpixel” design where the largest dimension of each red–green–blue combination is smaller than the resolution limit of the human eye. A three-dimensional rendering of such a device is shown in (c).

section of such a device is shown in Figure 5a. The top pane represents the output slits of the device and the bottom pane shows the input slits. The largest dimension of such a pixel would be  $\sim 3 - 5 \mu\text{m}$ . At present, this is 1–2 orders of magnitude smaller than the best high-definition color filters currently available.<sup>15</sup> Thus, these devices provide  $\sim 0.05\%$  transmittance through an individual device that is 2–3 orders of magnitude lower than traditional LCD color filters; the density of these devices in a two-dimensional array is 2–3 orders of magnitude higher than traditional LCD color filters. If instead of high resolution a higher transmission is required, the hexagonal pixels could be tiled together to form “superpixels”, as shown in Figure 5b. These structures could be designed such that the largest dimension is still smaller than the  $\sim 80 \mu\text{m}$  resolution limit of the human eye at 35 cm.<sup>18</sup> To maintain a uniform density of all three colors, the slit spacing can be kept constant over all devices and the different colors of each “superpixel” can be selected by simply varying the depth of that pixels’ output slits. For a given  $5 \mu\text{m}$  slit at a given wavelength within the superpixel structure, these devices provide between 0.02 and 0.1% transmission. A three-dimensional schematic of such a structure is shown in Figure 5c.

Metal–insulator–metal waveguides utilizing lithium niobate offer a unique opportunity for tunable light filters. By varying the spacing between the input and output slits, the intensity of a selected color oscillates as a function of the separation. Also, by varying the output slit depth within the device, one can preferentially couple to each of the photonic modes within the waveguide. The electro-optic effect of lithium niobate allows the selected output color to be shifted across the red, green, and blue regions of the

visible spectrum. Furthermore, these structures could produce color pixels that are orders of magnitude smaller than current technologies and could provide an opportunity for devices with a significantly higher resolution than those currently available.

**Acknowledgment.** This research was supported by the AFOSR Grant FA9550-06-1-0480 and ARO-MURI Grant W911NF-07-1-0410. We thank E. Feigenbaum and R. Briggs for engaging discussions. J.A.D. acknowledges support from the NSF and an NDSEG fellowship administered by the Army Research Office. M.S. acknowledges support from a NSF graduate research fellowship. This work was also supported by the Center for Science and Engineering of Materials, an NSF MRSEC.

**Supporting Information Available:** This material is available free of charge via the Internet at <http://pubs.acs.org>.

## References

- (1) Zia, R.; Selker, M. D.; Catrysse, P. B.; Brongersma, M. L. *J. Opt. Soc. Am. A* **2004**, *21*, 2442–2446.
- (2) Shimizu, K. T.; Pala, R. A.; Fabbri, J. D.; Brongersma, M. L.; Melosh, N. A. *Nano Lett.* **2006**, *6*, 2797–2803.
- (3) Dionne, J. A.; Lezec, H. J.; Atwater, H. A. *Nano Lett.* **2006**, *6*, 1928–1932.
- (4) Dionne, J. A.; Sweatlock, L. A.; Atwater, H. A.; Polman, A. *Phys. Rev. B* **2006**, *73*, 035407.
- (5) Liu, S. W.; Xiao, M. *Appl. Phys. Lett.* **2006**, *88*, 143512.
- (6) Park, H.-G.; Barrelet, C. J.; Wu, Y.; Tian, B.; Qian, F.; Lieber, C. M. *Nat. Photonics* **2008**, *2*, 622–626.
- (7) Laux, E.; Genet, C.; Skauli, T.; Ebbesen, T. W. *Nat. Photonics* **2008**, *2*, 161–164.
- (8) van Hulst, N. F. *Nat. Photonics* **2008**, *2*, 139–140.
- (9) Barnes, B.; Sambles, R. *Phys. World* **2006**, *19*, 17–21.
- (10) Fejer, M. M.; Magel, G. A.; Jundt, D. H.; Byer, R. L. *IEEE J. Quantum Electron.* **1992**, *28*, 2631–2654.
- (11) *Properties of Lithium Niobate*; INSPEC, Inc.: 2002.
- (12) CVRL Color & Vision Database, Colour & Vision Research Laboratories, Institute of Ophthalmology, UCL. <http://www.cvrl.org/>.
- (13) *Color science: concepts and methods, quantitative data and formulae*; Wiley: 1982.
- (14) Dionne, J. A.; Sweatlock, L. A.; Polman, A.; Atwater, H. A. *Phys. Rev. B* **2005**, *72*, 075405.
- (15) Lien, A.; Cai, C.; John, R. A.; Galligan, J. E.; Wilson, J. *Displays* **2001**, *22*, 9–14.
- (16) MTI Crystal Database. <http://www.mtixtl.com/>.
- (17) *Properties of Lithium Niobate*; The Institution of Engineering and Technology: 2002.
- (18) Betancourt, D.; del Rio, C. *IEEE Sensor Array Workshop* **2006**, 93–97.

NL900755B